Predictability of Stratospheric Ozone in the Southern Hemisphere during Spring

中村, 東奈

Predictability of Stratospheric Ozone in the Southern Hemisphere during Spring

NAKAMURA Haruna

Department of Earth and Planetary Sciences

Kyusyu University

February 2023

Abstract

A reduction of the total ozone over the southern tip of South America lasting 3 weeks occurred in November 2009. In this event, the polar vortex was distorted to an elliptic shape due to enhanced planetary wave activity, bringing to migration of ozone depletion region associated with the Antarctic ozone hole towards the South American continent at the time of the vortex breakup. We attempt ensemble forecast experiments for the ozone reduction event, using the National Institute for Environmental Studies (NIES) chemistry-climate model (NIES CCM) with 32 ensemble members whose initial data was produced by the ozone assimilated NIES CCM from the Modern-Era Retrospective analysis for Research and Applications, version 2 (MERRA-2) reanalysis data for the dynamical field, along with the Aura Ozone Monitoring Instrument (OMI) and Microwave Limb Sounder (MLS) data for the ozone field. The forecast experiments are performed from the various initial dates in October-November 2009.

To quantify the model performance, we investigate the predictability of the geopotential height and total ozone fields, on the basis of the pattern correlation coefficient (PCC) and Root Mean Square Error (RMSE) between their forecast and reanalysis values. It is found that the geopotential height and ozone fields are well

predictable prior to the ozone reduction event; the predictability limit of total ozone field for the lasting ozone reduction event in November is about 6 days, whereas the predictability limit for the temporally ozone reduction event is more than 10 days. It is found that the reproduction of upward propagation of wave activity flux emanated from a blocking anticyclone is a crucial factor for the successful forecast of the lasting ozone reduction event, and such complicated dynamical processes are considered to make the short predictability limit.

We also investigate the difference of the assimilated data for initial data for the forecast experiments. The difference of assimilated ozone data suggests the importance of the accuracy of vertical ozone profile at initial state.

Contents

1. Introduction

In the end of 1970s, the total ozone reduction was found over Antarctica. The phenomenon was named “ozone hole”, because it looked like a large hole of total ozone enough to cover Antarctica when viewed from satellite data. The ozone hole is a phenomenon in which the amount of total ozone over Antarctica is extremely depleted. It occurs in early austral spring and disappears in late spring or early summer.

The ozone depletion is caused by catalytic cycles involving chlorine and/or bromine species originated from anthropogenic ozone-depleting substances (ODS) such as chlorofluorocarbons (CFCs). During winter, the polar vortex becomes extremely cold due to weak planetary wave activity in the Southern Hemisphere and “polar stratospheric clouds” (PSCs), i.e., thin clouds of ice or liquid water particles can form in the Antarctic lower stratosphere. On the surface of the PSCs, chlorine compounds (Cl_2 and HOCl) can be released from the reservoir species such as $ClONO_2$ (chlorine nitrate) and HCl (hydrochloric acid) through heterogeneous reactions. In early spring, the Sun returns to the polar region and photolyze these chlorine compounds to provide a supply of Cl for the ozone depleting catalytic cycles, leading to the ozone hole. Bromine compounds are also considered to contribute to

the ozone depletion through similar chemical reactions. Finally, the ozone hole disappears with the breakup of the polar vortex.

In 1987, the Montreal Protocol, which stipulated regulations on ODS, was adopted, and efforts have been made to reduce them, but ozone hole still occurs every year and the recovery of stratospheric ozone to the level of 1980 is expected to be prolonged after 2050 (WMO, 2018).

On the other hand, the Antarctic ozone hole shows significant interannual variability in its magnitude and shape, which could be caused by both chemical and dynamical factors, such as changes of ODS amounts, planetary wave activity and polar vortex strength. The variation of the Antarctic ozone hole poses a UV risk for people living in the southern part of South America, as depletion of total ozone results in more UV rays reaching to the ground. In the Southern Hemisphere spring, it has been reported that the polar vortex is sometimes deformed to an elliptic shape by wave activity changes and passed over southern tip of South America, then causes temporary total ozone depletion at the area (Akiyoshi et al. 2018). During the Antarctic ozone hole season in 2009, the deformed Antarctic polar vortex stayed there in three weeks of November. This led to continuous small total ozone over the southern tip of South America and large UV index values (de Laat et al., 2010,

Wolfram et al., 2012). The time series of total ozone over Rio Gallegos, Argentina (51.5°S, 69.3°W) during the Antarctic ozone hole season in 2009 showed the small total ozone value below 250 DU lasted from middle to late November.

Akiyoshi et al. (2018) investigated this ozone reduction event and showed that the tropospheric blocking was maintained in November 2009, and the upward wave activity flux from the blocking to stratosphere occurred, leading to the elongation and the migration of the polar vortex.

As mentioned earlier, late spring in Southern Hemisphere corresponds to the breaking-up time of the polar vortex which has developed over Antarctica during winter. In that season, the stratospheric circulation changes drastically with large variability of the polar vortex, which sometimes leads to ozone reduction event over the southern tip of South America. Forecasting the change of Antarctic ozone hole is expected to help warning UV risk to people in high latitudes in the Southern Hemisphere, but the predictability of ozone field has not been investigated well. Furthermore, no studies have revealed the predictability limit of stratospheric ozone field using ozone forecasting models.

On the other hand, the forecast of dynamical field in the stratosphere has been investigated by many studies (e.g., Mukougawa and Hirooka, 2004; Mukougawa et

al., 2005; Hirooka et al., 2007; Kuroda, 2008; Stan and Straus, 2009; Ichimaru et al., 2014; Noguchi et al., 2014, 2016; Rao et al., 2019). Most of them dealt with predictability of sudden stratospheric warmings (SSW) events.

For example, Ichimaru et al. (2013) investigated the predictability of stratospheric circulations and SSW events in the Northern Hemisphere using the archive of 1-month ensemble forecast dataset by the Japan Meteorological Agency. They evaluated the predictability limit on the basis of Root Mean Square Error (RMSE) and Anomaly Correlation (AC) of the 10-hPa geopotential height in the Northern Hemisphere and showed that it was estimated to be about 10 days with a large variance. Noguchi et al. (2016) investigated the predictability limit for the period around a split-type SSW event in January 2009. Generally, it is difficult to predict the time evolution of stratospheric dynamical field around SSW events, especially for split-type SSWs. They showed that breakup of the polar vortex due to the SSW occurrence in the Northern Hemisphere could be predicted 6 days before.

The ozone field are affected by the variability of both dynamical and atmospheric chemical fields, so that its predictability limit may be shorter than that of dynamical fields. However, predictability of the ozone field has been investigated only by a small number of studies for limited cases based on chemical transport models (e.g.,

Sekiyama and Shibata, 2005; Flemming et al., 2011). Hence, the details are still unknown on this aspect. Furthermore, because current operational weather forecast models for weather do not include interaction between dynamical and chemical fields, plausible contributions of the chemical field to dynamical one is also unknown.

In this study, in order to reveal the precise predictability variation of Antarctic ozone field associated with time evolution of ozone hole in spring, we investigated two types of the ozone reduction events in 2009 using the chemistry-climate model (CCM). One event is the polar vortex deformed elliptically and passed over southern tip of South America, while the other one is the event of deformed Antarctic polar vortex stayed over the southern tip of South America in three weeks of November. The former may correspond to short-term UV risks due to rapid and temporary ozone depletion, and the latter may correspond the relatively long-term UV risks by the ozone hole staying over the southern tip of South America.

The CCM used in this study is based on the Model for Interdisciplinary Research on Climate MIROC version 3.2 (MIROC 3.2), which is developed by the National Institute for Environmental Studies (NIES). The NIES CCM includes the interaction between dynamical fields include radiation and chemical fields, so that the NIES CCM can reveal how the change of ozone field affect to dynamical fields. Hence, it

would be expected that predictability of dynamical fields may be better, if the NIES CCM can predict ozone fields well.

2. Theoretical Background

We make dynamical analyses to investigated plausible reasons bringing about differences of predictability limits in performed forecast experiments from various initial data, on the basis of the transformed Eulerian mean (TEM) equations (Andrews and McIntyre, 1976). The initial data are produced by the use of an assimilation method based on a Local Ensemble Transform Kalman Filter (LETKF) proposed by Hunt et al. (2007). Thus, we briefly review the quasi-geostrophic TEM equations and LETKF in this section.

2.1 The TEM equations

First, we describe the quasi-geostrophic TEM equations following Andrews et al. (1987). Here, a zonal average is denoted by an overbar, while a disturbance component is denoted by a prime which is obtained by removing the zonal averages at each latitude and height. The TEM set of equations can be shown in spherical log-pressure coordinates as follows:

$$\bar{u}_t - f\bar{v}^* - \bar{X} = (\rho_0\, a\cos\phi)^{-1}\nabla\cdot\mathbf{F}, \tag{2.1}$$

$$\bar{\theta}_t + \bar{w}^*\theta_{0z} - \bar{Q} = 0, \tag{2.2}$$

$$(a\cos\phi)^{-1}(\bar{v}^*\cos\phi) + {\rho_0}^{-1}(\rho_0\bar{w}^*)_z = 0, \tag{2.3}$$

$$f\bar{u}_z + \frac{R}{aH} e^{(-\kappa z/H)} \bar{\theta}_\phi = 0, \tag{2.4}$$

where $\bar{u}$ is the zonal mean zonal wind and $f = 2\Omega \sin\phi$ is Coriolis parameter. $\rho_0 = \rho_s e^{(-z/H)}$ is the basic density, H is the scale height and ϕ is latitude. θ is the potential temperature, and $\theta_0 = HR^{-1} e^{(-\kappa z/H)} \Phi_{0z}$ is the reference potential temperature. a, Ω, and R is the Earth' s radius, rotation rate and gas constant for dry air, respectively. $\bar{X}$ and $\bar{Q}$ denote the unspecified horizontal components of friction or other non-conservative mechanical forcing, and a diabatic heating term, respectively. $\kappa \equiv R/C_p$ is the ratio of gas constant to specific heat at constant pressure and C_p is the specific heat of dry air at constant pressure. $(\bar{v}^*, \bar{w}^*)$ is a residual mean meridional circulation defined as follows:

$$\bar{v}^* \equiv \bar{v} - {\rho_0}^{-1} (\rho_0 \, \overline{v'\theta'}/\bar{\theta}_z)_z, \tag{2.5}$$

$$\bar{w}^* \equiv \bar{w} + (a\cos\phi)^{-1} (\cos\phi \overline{v'\theta'}/\bar{\theta}_z)_\phi. \tag{2.6}$$

The vector $\mathbf{F}$ in eq. (2.1) is the Eliassen-Palm flux (EP flux).

The definition of the quasi-geostrophic EP flux in spherical and log-pressure coordinates is represented as follows:

$$\mathbf{F} \equiv [\mathbf{0}, -\rho_0 a \cos\phi \overline{v'u'}, \rho_0 a \cos\phi f \overline{v'\theta'}/\theta_{0z}]. \tag{2.7}$$

Note that the meridional and vertical components are related to eddy momentum flux and eddy heat flux, respectively.

As seen in eq. (2.1), eddy-forcing terms only appear explicitly in the mean zonal momentum equation as a form of the divergence of the EP flux, while the eddy forcing terms are not seen explicitly in the thermodynamic equation, eq. (2.2). Thus, note that the eddy momentum flux and eddy heat flux do not act separately but in the combination for the mean zonal wind driving in the TEM equations.

The EP flux can be related to wave activity density A under Wentzel-Kramers-Brillouin (WKB) conditions as follows (Edmon et al., 1980):

$$\mathbf{F} = \mathbf{c_g} A, \tag{2.8}$$

$$A = E/(\bar{u} - c), \tag{2.9}$$

where $\boldsymbol{c_g}$ is group velocity, E is wave energy density and c is phase velocity, respectively. Note that A is positive for planetary waves. Thus, the EP flux vector is proportional to the group velocity of planetary waves and represents the direction of wave energy propagation in the meridional plane.

Considering steady, linear and conservative (no frictional or diabatic) waves on a basic zonal flow, we can show the Eliassen-Palm theorem that the divergence of the EP flux becomes zero. This theorem was first shown in in a pioneering paper by Eliassen and Palm (1961). In this case, we can derive the nonacceleration theorem that mean zonal winds and temperatures are unchanged for the conservative flow.

This relationship was first noted by Charney and Drazin (1961).

The Eliassen-Palm theorem can be extended to a more generalized case, i.e., the generalized Eliassen-Palm theorem defined by:

$$\frac{\partial A}{\partial t} + \boldsymbol{\nabla} \cdot \mathbf{F} = D + O(\alpha^3), \tag{2.10}$$

where the time derivative of A represents wave-transience effects. D represents the quantity accounts for frictional and diabatic effects, and $O(\alpha^3)$ is nonlinear wave effects.

The quasi-geostrophic beta-plane EP fluxes are given by:

$$\mathbf{F} \equiv [0, -\rho_0 \overline{v'u'}, \rho_0 f_0 \overline{v'\theta'}/\theta_{0z}]. \tag{2.11}$$

For further discussion of TEM equations see, e.g. Andrews et al. (1987).

2.2 LETKF: A local ensemble transform Kalman filter

A Local Ensemble Transform Kalman Filter (LETKF) was proposed by Hunt et al. (2007) and now widely used for the data assimilation. Here, we will briefly recall the LKTKF scheme. The LETKF scheme separates an entire grid vector into local patch vectors, and each local patch is treated independently. The forecast error covariance matrix $\mathbf{P}^f$ are given by

$$\mathbf{P}^f = \mathbf{E}^f \tilde{\mathbf{P}}^f \left(\mathbf{E}^f\right)^T, \tag{2.12}$$

where $\mathbf{E}$ denote $N \times m$ matrix; m ensemble perturbations (ensemble members) of an N-dimensional local patch. $\mathbf{E}^f$ gives the mapping from the m-dimensional space to N-dimensional physical space. $\widetilde{\mathbf{P}}^f$ is forecast error covariance matrix (m-dimension) in the space spanned by forecast ensemble perturbations and described as follows:

$$\widetilde{\mathbf{P}}^f = (m-1)^{-1}\mathbf{I}. \tag{2.13}$$

The analysis error covariance matrix is described as follows:

$$\widetilde{\mathbf{P}}^a = \left[\left(\mathbf{H}\mathbf{E}^f\right)^T \mathbf{R}^{-1}\mathbf{H}\mathbf{E}^f + (m-1)^{-1}\mathbf{I}/\Delta\right]^{-1}, \tag{2.14}$$

where $\mathbf{H}$ and $\mathbf{R}$ are the linear observational operator and observational error covariance matrix, and Δ denotes covariance inflation parameter.

The linear observational operator $\mathbf{H}$ in eq. (2.14) is approximated by a nonlinear observational operator H:

$$\mathbf{H}\delta\mathbf{x} \approx H(\bar{\mathbf{x}} - \boldsymbol{\delta}\mathbf{x}) - H(\bar{\mathbf{x}}), \tag{2.15}$$

where $\bar{\mathbf{x}}$ and $\boldsymbol{\delta}\mathbf{x}$ are an ensemble mean and perturbation. The analysis increment in the m-dimensional space is

$$\delta\tilde{\mathbf{x}}^a = \widetilde{\mathbf{P}}^a\left(\mathbf{H}\mathbf{E}^f\right)^T \mathbf{R}^{-1}\mathbf{d}, \tag{2.16}$$

where $\mathbf{d}$ is the observational increment. The analysis ensemble perturbations in m-dimensional space are

$$\tilde{\mathbf{E}}^a = \left[(m-1)\tilde{\mathbf{P}}^a\right]^{1/2}. \tag{2.17}$$

The final analysis ensemble members in the N-dimensional physical space is given by mapping with $\mathbf{E}^f$:

$$\left[\mathbf{x}^{a(1)}|\cdots|\mathbf{x}^{a(m)}\right] = \left[\bar{\mathbf{x}}^f|\cdots|\bar{\mathbf{x}}^f\right] + \mathbf{E}^f\left([\delta\tilde{\mathbf{x}}^a|\cdots|\delta\tilde{\mathbf{x}}^a] + \tilde{\mathbf{E}}^a\right) \tag{2.18}$$

where $\bar{\mathbf{x}}^f$ is the forecast ensemble mean state.

3. Data and Model

We attempt ensemble forecast experiments for the ozone reduction event, using NIES CCM with 32 ensemble members whose initial values were produced by the Ozone Assimilated NIES CCM (Nakamura et al., 2013). For forecasting dynamical and chemical fields using atmospheric numerical models, it is important to start calculations from initial values that are as close as possible to the actual fields. There are various methods to obtain initial values close to the real fields, and we choose to create initial values by the data assimilation method. The Ozone Assimilated NIES CCM is an ozone assimilation system applying a four-dimensional local ensemble transform Kalman filter (LETKF; Hunt et al., 2007). The data assimilation system is divided into the forecast step and assimilation step. In the forecast step, the model forecasts are made for each ensemble member, while in the assimilation step, observational data assimilation is performed for each ensemble member. The ensemble mean value of assimilated data is called “analysis data”. We use each assimilated data as initial data for ensemble forecasts.

The model integration of NIES CCM and the assimilation are performed with triangular 42 truncation (T42) and 34 vertical levels up to 0.01 hPa. The model variables used for assimilation are zonal wind velocity (U), meridional wind velocity

(V), temperature (T) and the ozone volume mixing ratio (XO3). The observational variables are 3 types; dynamical fields (U, V, T), ozone profile (XO3) and total ozone (TO3) fields. The dynamical fields are given by the Modern-Era Retrospective analysis for Research and Applications, version 2 (MERRA-2) reanalysis data (Gelaro et al., 2017). The Aura Ozone Monitoring Instrument (OMI) data (McPeters et al., 2008) are used for the total ozone field and Microwave Limb Sounder (MLS) data (Livesey et al., 2022) are used for the ozone profile.

The cycle of the assimilation system in the Ozone Assimilated NIES CCM is as follows. In the forecast step, a 1-day (from 00UTC to 24UTC) forecast integration is performed for 32 ensemble members from different initial states. After 1-day forecasts for 32 ensemble members, observational data assimilation is performed to every 6 hours forecasts and obtain “analysis data”. The final timestep (24 UTC) of assimilated fields are used for the initial value for the next 1-day forecast. We performed data assimilation by the use of the Ozone Assimilated NIES CCM for 1 September to 30 November, and we obtain the initial data for forecast experiments.

After performing the Ozone Assimilated NIES CCM, the forecast experiments are made from the various initial dates in September to November 2009. As mentioned in Section 1, we focus on the two ozone reduction events over the southern tip of

South America. For the temporal ozone reduction event caused by the elliptically deformed polar vortex, the initial dates for forecast experiments are set from 28 September to 1 October. For the relatively long ozone reduction event lasting three weeks caused by the polar vortex staying over the southern tip of South America, the initial dates are set from 5 to 10 November. Each forecast experiments are performed for 10 days.

Figure 3-1 shows the time evolution of total ozone at the southern tip of South America, Rio Gallegos, Argentina (51.5°S, 69.3°W) during the 2009 Antarctic ozone hole season. It shows the small total ozone value below 250 DU lasts from middle to late November which corresponds to the polar vortex staying event. It also shows the temporal total ozone depletion at the end of September and the beginning of October, which corresponds to the elliptically deformed polar vortex event.

Figure 3-2 shows total ozone maps in the Southern Hemisphere at the ozone reduction events. The polar map when temporally total ozone depletion occurred over the southern tip of South America (4 October in 2009) shows the elliptically deformed polar vortex (Figure 3-2a), while the polar map when the total ozone reduction lasted shows the migration of the deformed polar vortex (Figure 3-2b).

We also investigated the variation of total ozone in spring at Rio Gallegos,

Argentina for 30 years (1980-2010). It is found that there is no year in which continuous small ozone values lasted over the southern tip of South America like in November 2009, although ozone hole stayed over other longitudes in some years.

(a) NIES CTM

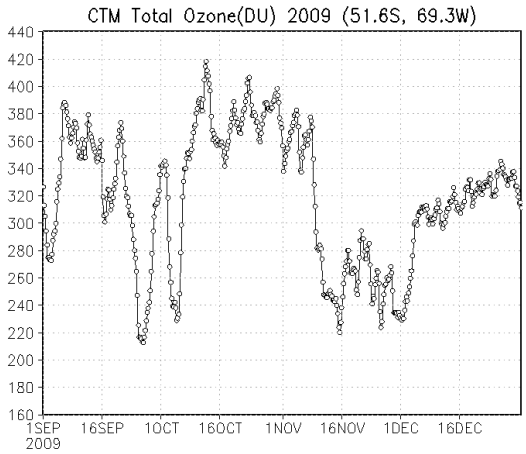

(b) OMI

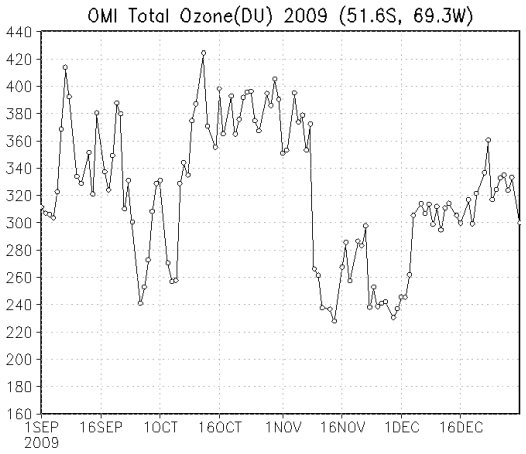

Figure 3-1: Time series of the total ozone which is (a) calculated by NIES CTM and (b) OMI observational data over Rio Gallegos, Argentina (51.5°S, 69.3°W) from September to December, 2009. Units are DU.

(a) 10/4

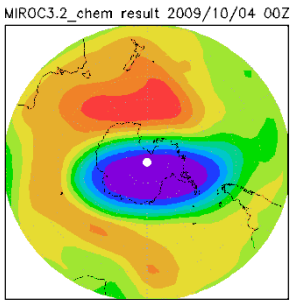

(b) 11/20

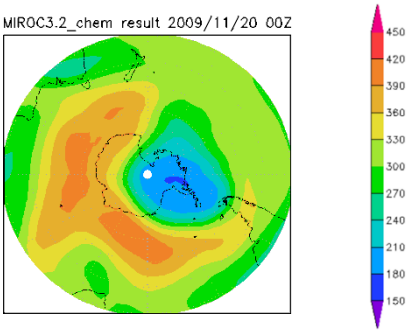

Figure 3-2: Total ozone of (a) 4 October and (b) 20 November, 2009 calculated by NIES CTM. Units are DU.

4. Analysis Methods

We here explain the definitions of Pattern Correlation Coefficient (PCC) and Root Mean Square Error (RMSE) and Ensemble Spread. These measures are used for our analysis.

4.1 PCC Analysis

PCC analysis is based on Anomaly Correlation (AC). AC or PCC indicates a measure of similarity of synoptic patterns.

The PCC at a forecast time t is defined as the following equation:

$$PCC(t) = \frac{\sum_{i=1}^{n} w(i)\left[z_{fc}(i,t) - \overline{z_{fc}(t)}\right]\left[z_{ra}(i,t) - \overline{z_{ra}(t)}\right]}{\sqrt{\sum_{i=1}^{n} w(i)\left[z_{fc}(i,t) - \overline{z_{fc}(t)}\right]^2}\sqrt{\sum_{i=1}^{n} w(i)\left[z_{ra}(i,t) - \overline{z_{ra}(t)}\right]^2}}, \quad (1)$$

where z_{fc} and z_{ra} indicate each forecast and observation of physical fields (geopotential height and total ozone) on the i-th grid point, respectively. n is the number of grid points in the Southern extratropics (poleward of 20°S). The overbars in equation (1) denote spatial average, including latitude weighting:

$$\overline{z(t)} = \frac{\sum_{i=1}^{n} w(i)\, z(i,t)}{\sum_{i=1}^{n} w(i)}, \quad (2)$$

where $w(i)$ represents the cosine of latitude on the i-th grid point. In general, the predictability limit is defined as the time when the AC or PCC first drops to 0.6 (e.g., Hollingsworth et al. 1978).

4.2 RMSE Analysis

The RMSE at a forecast time t is defined as the following equation:

$$\sigma(t) = \left[\frac{\sum_{i=1}^{n} \left(z_{fc}(i,t) - z_{ra}(i,t) \right)^2 w(i)}{\sum_{i=1}^{n} w(i)} \right]^{\frac{1}{2}}, \tag{3}$$

where z_{fc} and z_{ra} indicate each forecast and observation of physical fields on the i-th grid point, respectively. n is the number of grid points and $\sigma(t)$ is averaged over latitudes south of 20°S. The RMSE indicates a mean distance between forecasts and observations, so that it means an average forecast error.

In general, the predictability limit is defined as the time when the RMSE first surpasses a specified criterion which represents the magnitude of natural variability in the considered field. For example, in the troposphere a climatological standard deviation (CSD) is used as a threshold. The CSD is defined as the following equation:

$$\sigma_c = \left[\frac{\sum^{D} \sum_{i=1}^{n} \left(z_{ra}(i,t) - z_c(i,t) \right)^2 w(i)}{D \sum_{i=1}^{n} w(i)} \right]^{\frac{1}{2}}, \tag{4}$$

where z_c represents the climatological mean value on the i-th grid point and D is a long duration defining climatology, respectively.

4.3 Ensemble Spread

The ensemble spread at each grid point is defined as the following equation:

$$Spread(i,t) = \sqrt{\frac{1}{M}\sum_{j}^{M}\left(z_j(i,t) - z_{me}(i,t)\right)^2}, \quad (5)$$

where M is the number of ensembles, z_j is forecasted physical field at j-th ensemble member and z_{me} is the mean value of ensembles, respectively. The Ensemble Spread indicates a distance between each ensemble member and ensemble mean, so that it means the variability of the ensemble forecasts.

5. Predictability of Stratospheric Ozone from Various Types of Initial Data

5.1 Initial Data for the Forecast Experiments

To attempt ensemble forecast experiments for the ozone reduction events, we produced three types of initial data using the ozone assimilated NIES CCM: U, V and T (zonal winds, meridional winds, and temperatures) assimilated initial data (UVT-ini), U, V, T and total ozone assimilated initial data (UVT-TO3-ini), and U, V, T, total ozone and ozone volume mixing ratio profile assimilated initial data (UVT-TO3-XO3-ini). Note that the ozone volume mixing ratio profile (hereafter, ozone profile) is a function of altitude.

We expect the two types of ozone assimilated initial data are better (similar to observational data) than UVT-ini, because it is expected that the correct distribution of ozone will be able to accurately reproduce radiative effects of ozone fields to dynamical fields.

We also expect UVT-TO3-XO3-ini is better than UVT-TO3-ini. Figure 5-1 shows the schematic image of the assimilation of UVT-TO3-ini (Figure 5-1a) and UVT-TO3-XO3-ini (Figure 5-1b). The UVT-TO3-ini (Figure 5-1a) is collected the amount of total ozone without a change of its profile, whereas UVT-TO3-XO3-ini (Figure 5-1b) is

corrected its ozone profile to be consistent with both observed total ozone and ozone profile. Then, the total ozone of UVT-TO3-ini is expected to be consistent with observed total ozone (OMI), but its profile may not be consistent with observed one.

Figure 5-2 plots the time series of total ozone of three types of initial data and OMI (gray line) over Rio Gallegos, Argentina (51.5°S, 69.3°W) from 6 to 17 November, 2009. The UVT-TO3-ini (green line) and the UVT-TO3-XO3-ini (red line) reproduce the ozone reduction event from 9 November, while the total ozone reduction of UVT-ini (blue line) is not enough compared to other two types of initial data.

5.2 The Forecast Experiments from Various Types of Initial Data

We attempt to ensemble forecast experiments for ozone reduction events using NIES CCM. The initial data are the three types of assimilated fields described in Subsection 5.1. We set the forecast period from 6 to 15 November, 2009 to target the beginning of the Migration of the polar vortex event from 10 to 30 November 2009 (see Section 3).

Figure 5-3 shows the polar maps of OMI and ensemble mean of total ozone of the forecast experiments over the Southern Hemisphere during the forecast period. The experiments using UVT-ini (UVT-ex) show higher total ozone inside the polar vortex

(correspond to blue color area) than other two types of experiments overall the period. On the other hand, the shapes of the polar vortex of UVT-ex are consistent with those of OMI total ozone. The experiments using UVT-TO3-ini (UVT-TO3-ex) and the experiments using UVT-TO3-XO3-ini (UVT-TO3-XO3-ex) represent the total ozone inside polar vortex and their deformation well. The shapes of the polar vortex of UVT-TO3-ex after 10 November slightly deviate from that of OMI and UVT-TO3-XO3-ex.

We also investigate the reproducibility of total ozone over the southern tip of South America. Figure 5-4 shows the time series of total ozone of the ensemble mean of forecast experiments whose initial data are the three types of initial data, along with OMI observational data (gray line) over Rio Gallegos, Argentina (51.5°S, 69.3°W) from 6 to 15 November, 2009. The UVT-ex (blue line) shows higher total ozone values than those of OMI and other two experiments with a similar tendency to the results for synoptic features (Fig. 5-3). The UVT-TO3-ex reproduces the total ozone reduction on 14 November, but the beginning of the reduction is later than OMI. The UVT-TO3-XO3-ex shows the best timing of the total ozone reduction with slightly later than OMI. The difference between UVT-TO3-ex and UVT-TO3-XO3-ex is considered to be caused by the difference of deformation of the polar vortex in each

experiment.

5.3 Predictability Limit Based on PCC

To measure forecast skill, we calculate Pattern Correlation Coefficient (PCC) between forecast and reanalysis over south of 20°S, as described in Subsection 4.1, which is a measure of the similarity of synoptic patterns between the forecast and the reanalysis in the phase space. Figure 5-5 shows the time evolutions of total ozone PCC for 32 ensemble forecasts during the forecast period. Here, a threshold value in the stratosphere is set to 0.6, which is the same value as commonly used in the troposphere. If the PCC score shows 1.0, it means perfect skill. Generally, the PCC score decreases with forecast time. As mentioned in Subsection 4.1, the time when the PCC first reaches the threshold is defined as a predictability limit (Kalnay 2003), then we define the predictability limit as the time when the first member reaches the threshold PCC value. The time series of the evolution of PCC in UVT-ex (Figure 5-5a) are varied from the initial time, although its forecast limit is longer than 10 days. The time series in UVT-TO3-ex (Figure 5-5b) show good predictability until 10 November, but three members surpass the threshold (PCC=0.6) on 15 November, then its predictability limit is 9 days. The time series in UVT-TO3-XO3-ex (Figure

5-5c) show the best predictability in the three types and its predictability limit is longer than 10 days.

5.4 Predictability Limit Based on RMSE

Next, we measure forecast skill from another aspect using Root Mean Square Error (RMSE) in forecast members, as described in Subsection 4.2, which is a measure of the distance between the forecast and the reanalysis in the phase space. Figure 5-6 shows the time evolutions of total ozone RMSE for 32 ensemble forecasts during the forecast period. The values of RMSE in UVT-ex (Figure 5-6a) vary from 13 DU to 23 DU at the initial time, while those at the final state vary from 22 DU to 32 DU; thus the variability of each ensemble member shows little change. The time series in UVT-TO3-ex (Figure 5-6b) show small variability and small RMSE (about 12 DU) at the initial time, but they show higher variability than those in UVT-ex at the final state whose RMSE vary from 27 DU to 44 DU. The time series of UVT-TO3-XO3-ex (Figure 5-6c) show the smallest RMSE values and variability in the three types. The initial RMSE values are about 12 DU and those at the final state vary from 18 DU to 26 DU.

5.5 Discussion of Predictability from Various Types of Initial Data

Features of the total ozone forecast from various initial data of the three types have been investigated above.

The polar maps of total ozone (Figure 5-3) show small difference between UVT-TO3-ex and UVT-TO3-XO3-ex, and UVT-ex show higher total ozone than the observation and other two experiments. On the other hand, UVT-TO3-ex show higher variability than other two experiments from viewpoints of PCC and RMSE. In both the UVT-TO3-ini and the UVT-TO3-XO3-ini ozone fields are assimilated, though in the UVT-TO3-ini ozone fields are only assimilated without correction of its vertical profile. Then, the profile of UVT-TO3-ini would not be consistent with observational (real) ozone profile. The radiative effects of ozone to dynamical fields are maximized in the middle of stratosphere, so that the worsening of PCC and RMSE in UVT-TO3-ex suggests the importance of the accuracy of total ozone profile at the initial state.

In this section, we have obtained the result that UVT-TO3-XO3-ex shows good predictability for the ozone reduction event and its predictability limit estimated more than 10 days. Hence, we attempt to additional ensemble forecast experiments for UVT-TO3-XO3-ex for 20 days. Figure 5-7 shows the time evolutions of total ozone

PCC for 32 ensemble forecasts for 20 days, whose initial times are same as UVT-TO3-XO3-ex. The predictability limit is estimated 12 days because 18 November is the time when the PCC first reaches the threshold (PCC=0.6). We use UVT-TO3-XO3-ini for the forecast experiments to further investigate the predictability in the next section.

(a) UVT+TO3 (b) UVT+TO3+XO3

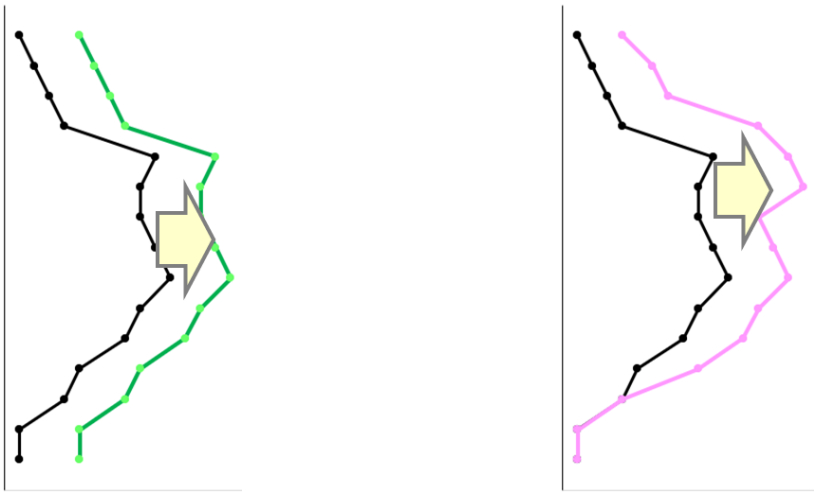

Figure 5-1: Schematic image of the correction of ozone profile by ozone assimilation. The black profiles indicate the ozone profile before assimilation. The green profile in (a) indicates the total ozone assimilated profile. The pink profile in (b) indicates the total ozone and ozone profile assimilated profile.

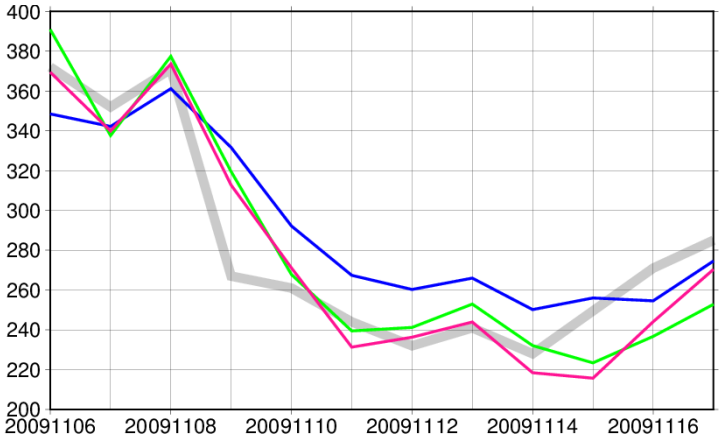

Figure 5-2: Time series of the total ozone (DU) which are initial data for forecast experiments and OMI observational data (gray line) over Rio Gallegos, Argentina (51.5°S, 69.3°W) from 6 to 17 November, 2009. Each initial data is calculated by the ozone assimilated NIES CCM. Blue, green and red line denote the time series of UVT-ini, UVT-TO3-ini and UVT-TO3-XO3-ini, respectively.

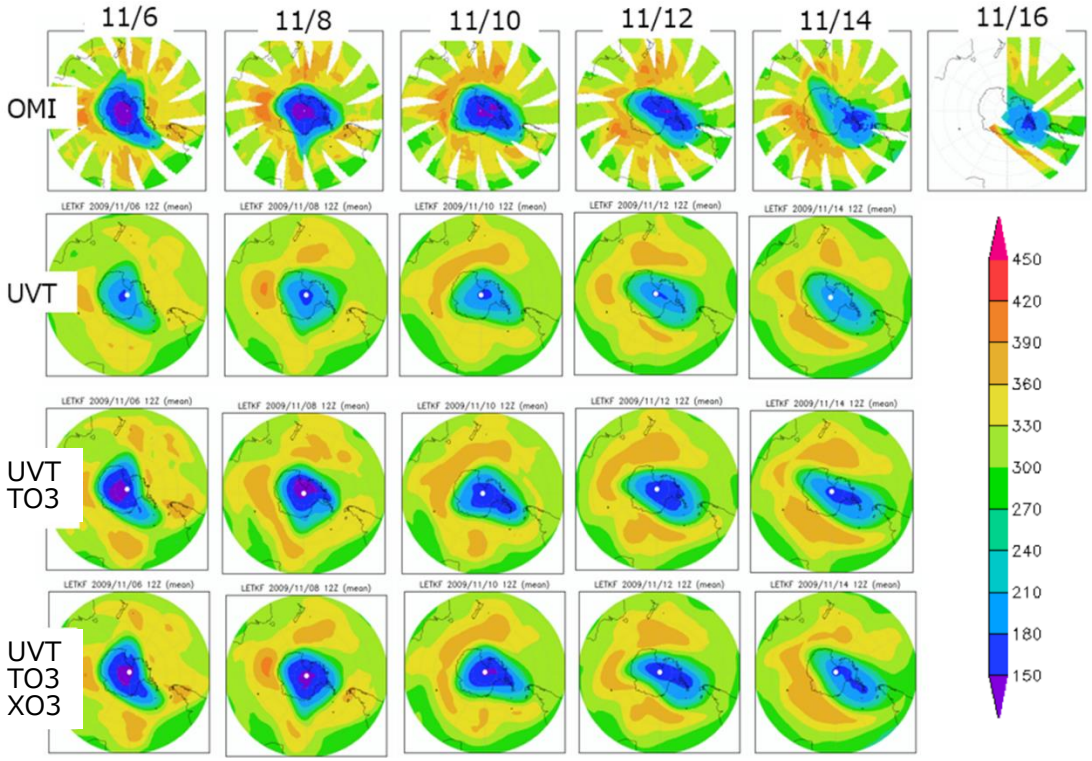

Figure 5-3: Total ozone for the period of 6-16 November, 2009. Top panels show OMI observational data, and second, third, bottom panels show ensemble mean of forecast experiments UVT-ex, UVT-TO3-ex, UVT-TO3-XO3-ex. Units are DU.

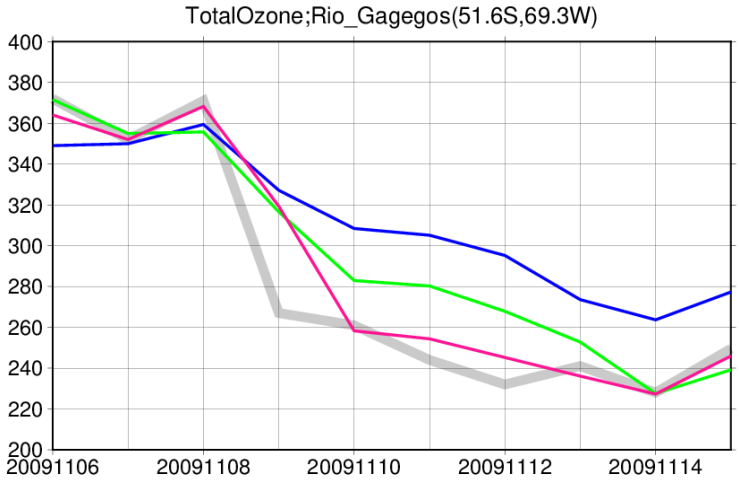

Figure 5-4: Time series of the total ozone (DU) of forecast experiments and OMI observational data (gray line) over Rio Gallegos, Argentina (51.5°S, 69.3°W) from 6 to 15 November, 2009. Blue, green, and red line denote the time series of UVT-ex, UVT-TO3-ex and UVT-TO3-XO3-ex, respectively.

(a) UVT

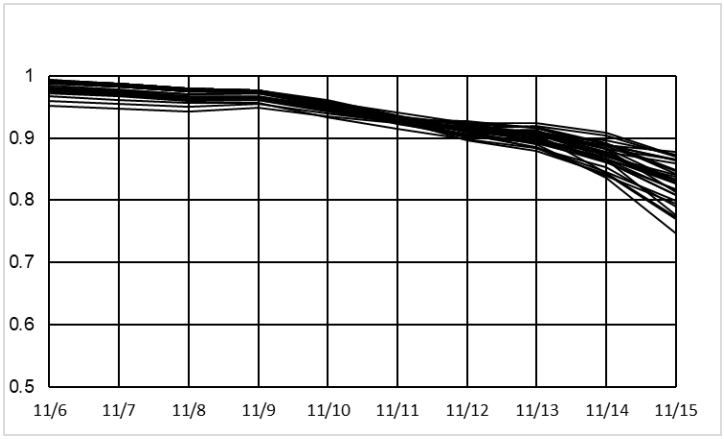

(b) UVT+TO3

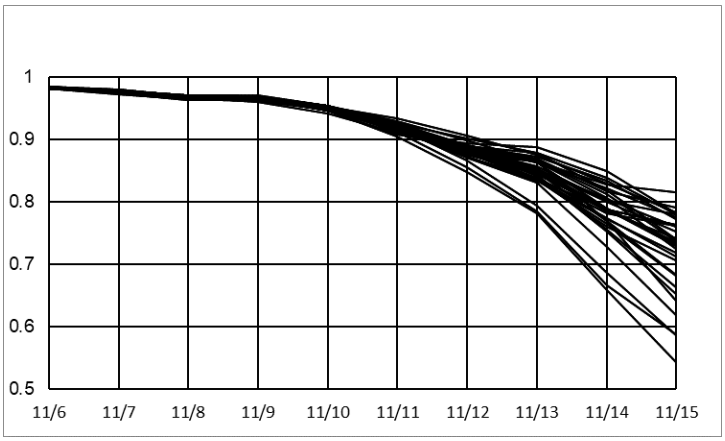

(c) UVT+TO3+XO3

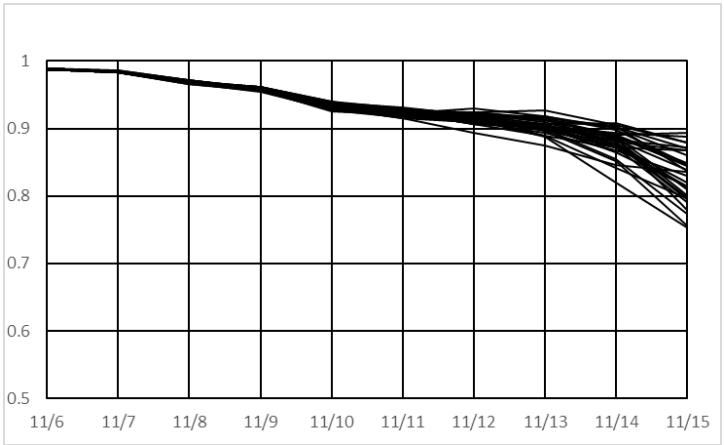

Figure 5-5: Time evolution of the PCC for 32 ensemble forecasts of total ozone (DU) for (a) UVT-ex, (b) UVT-TO3-ex and (c) UVT-TO3-XO3-ex during forecast period (6-15 November, 2009)

(a) UVT

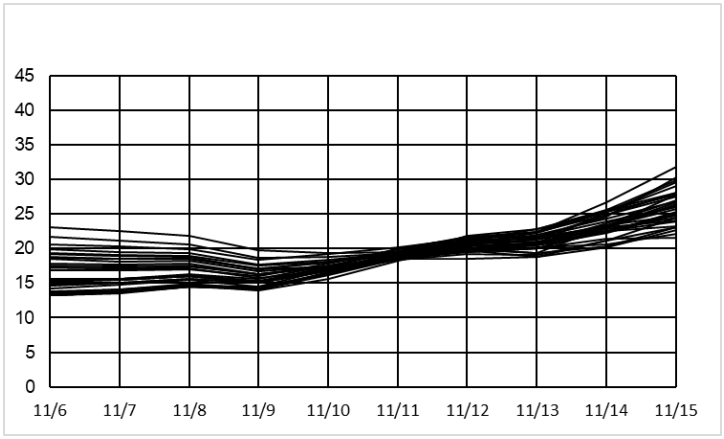

(b) UVT+TO3

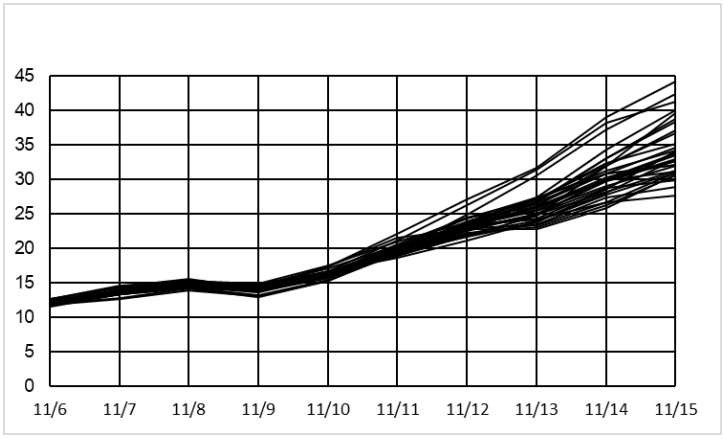

(c) UVT+TO3+XO3

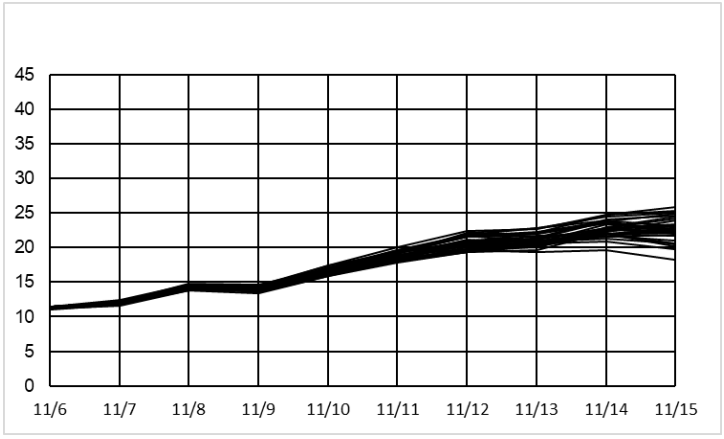

Figure 5-6: Time evolution of the RMSE for 32 ensemble forecasts of total ozone (DU) for (a) UVT-ex, (b) UVT-TO3-ex and (c) UVT-TO3-XO3-ex during forecast period (6-15 November, 2009)

UVT+TO3+XO3

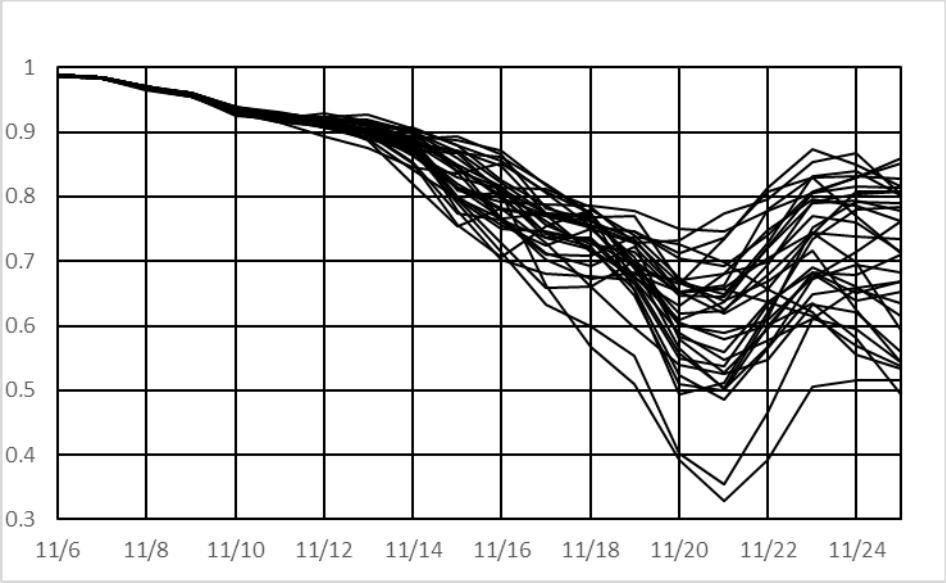

Figure 5-7: Same as Figure 5-5c but its forecast period is 6-25 November, 2009)

6. Predictability of Stratospheric Ozone from Various Initial Days

6.1 Initial Days for the Forecast Experiments

To compare two ozone reduction events of forecast experiments, we produced ensemble forecast experiments from various initial days using NIES CCM. One is a target to the Elliptic Shape of the polar Vortex event (ESV event) from 28 September to 5 October 2009, then the initial dates are set from 28 September to 1 October 2009. The other is a target to the Migration of the polar Vortex event (MV event) from 10 November to 30 November 2009, then the initial dates are set from 5 to 10 November 2009.

6.2 The Forecast Experiments from Various Initial Days

Figure 6-1 shows total ozone maps in the Southern Hemisphere based on OMI observations and ensemble mean of the forecast experiments during the forecast period. Although the forecast experiments for ESV event (Figure 6-1a) reproduce the elliptical deformation of the polar vortex and the amount of total ozone inside the polar vortex well, the forecasts with an initial date on 28 September show somewhat smaller deformation than the OMI total ozone and other forecasts, around 4 October.

On the other hand, the forecast experiments for MV event (Figure 6-1b) also reproduce the amount of total ozone inside polar vortex and their deformation generally well, but the experiments with initial dates on 8 and 10 November show smaller deformation around 12 and 14 October than the OMI total ozone and the forecast experiments with an initial date on 6 November.

6.3 Predictability Limit Based on PCC

To measure forecast skill, we calculate PCC between forecast and reanalysis over south of 20°S, as in Subsection 5.3.

Figure 6-2 shows the time evolutions of total ozone PCC for 32 ensemble forecasts during the forecast period. The threshold value set to 0.6, and we define the predictability limit as the time when the PCC first reaches the threshold. The time series of total ozone PCC for ESV event (Figure 6-2a) decrease slightly with time, and its forecast limit is longer than 10 days. Figure 6-2a also shows the total ozone PCC for the forecasts with initial dates on 28 and 29 September (green and blue lines in Figure 6-2a) greatly decrease after 5 October.

On the other hand, the total ozone PCC for MV event (Figure 6-2b) significantly decrease after 14 November. This indicates the forecast skills have deteriorated after

this day. Figure 6-2b also shows the predictability limits with initial dates on 5, 6 and 7 November are longer than 10 days, while the predictability limits with initial dates on after 7 November are shorter than 10 days (the shortest limit is about 6 days). Therefore, it can be concluded that the predictability limits are shorter for newer initial dates in this case. Similar results were reported by Kuroda (2010) for the experiment associated with sudden stratospheric events in the Northern Hemisphere. This kind of high initial-time sensitivity for the prediction is considered to result from high nonlinearity of atmospheric circulation changes. More studies are needed on this point in the future.

Figure 6-3 shows the same as Fig.6-2 but for the 50-hPa geopotential height field. The overall features of the time series of PCC are similar to the total ozone field. On the other hand, its predictability limit is longer than the total ozone field (more than 10 days).

6.4 Predictability Limit Based on RMSE

Next, we investigate forecast skill from the other side using RMSE in the forecast members same as in Subsection 5.4. Figure 6-4 shows the time evolutions of the total ozone RMSE for the 32 ensemble forecasts during the forecast period. The values of

RMSE of ESV event (Figure 6-4a) are about 20 DU at the initial date, and show smaller values for the forecast experiments with later initial dates than the forecast experiments with earlier initial dates. The values of RMSE of MV event (Figure 6-4b) are smaller (about 10 DU) than ESV event at the initial date. In comparison between the forecasts of MV event, the value of RMSE show larger values for the forecast experiments with later initial dates (8, 9 and 10 November) than the forecast experiments with earlier initial dates (5, 6 and 7 November). The total ozone RMSE for MV event (Figure 6-4b) significantly increase after 14 November. This indicates the forecast skills have deteriorated after this day, the tendency is as the same as the result of the PCC analysis.

6.5 Polar Vortex and Wave Activity.

Here, we focus on planetary wave activity of wavenumbers 1 and 2 to consider the predictability of two events. Figure 6-5 shows the schematic image of the correspondence between the polar vortex and planetary wave activity of wavenumbers 1 and 2. The enhanced planetary wave activity of wavenumber 1 contributes to the displacement of the polar vortex (Figure 6-5a), while wavenumber 2 contributes to the elliptic deformation of the polar vortex (Figure 6-5b).

Figure 6-6 shows the longitude-time section of the total ozone at 60°S during ESV event. The reanalysis data (Figure 6-6a) show the enhancement of wavenumber 1 and the rapid weakening of wavenumber 2 after 5 October. On the other hand, the forecasts with initial times on 28 September (Figure 6-6b) do not reproduce these features. The reproducibility of the change of planetary wave activity may affect especially to the deformation of the polar vortex leading to the decrease of PCC and increase of RMSE after 5 October.

Figure 6-7 shows the same as Fig.6-6 but for MV event. The reanalysis data show the enhancement of wavenumbers 1 and 2 around 14 November, and these phases almost stay at the same place (see Figure 6-7a). Although the forecasts with an initial date on 6 November (Figure 6-7b) reproduce these features, their amplitudes are slightly weaker than the reanalysis results. On the other hand, the forecasts with an initial date on 8 November (Figure 6-7c) show weak amplitudes throughout the period. Figure 6-8 shows the same as Fig.6-7 but for the 50 hPa geopotential height field. The overall features of the geopotential height field are similar to the total ozone fields. The reproducibility of the enhancement of planetary wave activity would affect the reproducibility of the displacement and deformation of the polar vortex, leading to the decrease of PCC and increase of RMSE after 14 November.

6.6 Features of EP flux during Ozone Reduction Event

To reveal plausible causes of the difference of wave activity between the forecast experiments, we investigate the vertical structure of dynamical fields using EP flux as described in Subsection 4.1. Figure 6-9 shows meridional cross sections of EP flux with vectors, its convergence with color shadings and zonal mean zonal winds with contours during MV event. The panels of Figures 6-9a, 6-9b, and 6-9c show the upward EP flux form the troposphere to the lower stratosphere (from 500 hPa to 100hPa) around 60°S. The forecast experiments with an initial date on 6 November (Figs. 6-9d, e, f) shows apparent vertical EP flux vectors in these areas as in the reanalysis results (Figs. 6-9a, b, c). On the other hand, the experiments with an initial date on 8 November (Figs. 6-9g, h, i) shows upward EP flux vectors in these areas on 9 and 10 November, but they become almost 0 value above 250 hPa on 11 November.

According to Akiyoshi et al. (2018), on 9 November, the upward wave activity flux vectors from the troposphere to the stratosphere were apparent around 60°S, 120°W. Hence, the upward EP flux vectors seen in Figure 6-9, which corresponds to this upward propagating feature of wave activity flux vectors, are considered to strongly influence the reproductivity of wave activity, therefore the predictability in the

stratosphere. In general, a blocking anticyclone has a barotropic structure and emanated EP and wave activity fluxes from it cannot propagate upward but propagate horizontally. In contrast, in the case of a blocking anticyclone slightly tilted westward with height, as observed in the beginning of the ozone reduction event (Akiyoshi et al., 2018), emanated fluxes can propagate upward. Our results clearly show that the reproduction of this feature is important for the high predictability.

6.7 The Features of Ensemble Spread during Ozone Reduction Event

We also investigate the ensemble spread of the geopotential height field during MV event to reveal the origin of the difference of predictability limits depending on initial dates for forecast experiments. The definition of the ensemble spreads is as described in Subsection 4.3. The area where the ensemble spreads are large corresponds to that with large variance.

Figure 6-10 shows the longitude-height section of ensemble spreads of the geopotential height field averaged over 50°S to 70°S. The large spread area raises around 120°W in the troposphere on 5 days after the initial date (Figure 6-10a, Figure 6-10b), and extends to 60°W of stratosphere on 7 days after the initial date in

the forecasts with an initial date on 8 November (Figure 6-10f). On the other hand, the large spread areas seem to be developed within the troposphere on 7 days after the initial day in the forecasts with an initial date on 6 November (Figure 6-10e).

Figure 6-11 shows the polar maps of the ensemble spreads of the geopotential height field at 50 hPa on 7 days after the initial day. The large spread areas extend along the edge of polar vortex. The values of the ensemble spread in the forecasts with an initial date on 8 November (Figure 6-11b) are larger than those of the forecasts with an initial date on 6 November (Figure 6-11a).

The features in ensemble spread analysis are consistent with the small variability of PCC and RMSE at the forecasts with an initial date on 6 November (Figure 6-2b). These features also indicate that the source of forecast error appears around 120°W in the troposphere; it has been reported that the area corresponds to a tropospheric blocking stayed at Atlantic Ocean (Akiyoshi et al., 2018).

6.8 Discussion of Predictability from Various Types of Initial Days

In general, it is expected that the closer to the target day (start of the ozone reduction event), the further the predictability will be improved. In fact, the forecast for ESV event shows better predictability at the later initial day. On the other hand,

the forecast for MV event show different features. The predictability significantly decreases after the specific day, i.e., 14 November in 2009 in each forecast. The upward propagating wave activity emanated from the tropospheric blocking area reaches the middle stratosphere by 14 November in 2009 (Akiyoshi et al., 2018), which caused the amplification of wavenumbers 1 and 2 in the stratosphere, leading to the displacement and deformation of the polar vortex.

As discussed in Subsection 6.6, the blocking anticyclone in this event showed a somewhat baroclinic feature with a westward phase tilt with height in this case, which makes the upward propagation of wave activity possible. Similar upward propagation of wave activity emanated from a blocking anticyclone was reported by Harada et al. (2010) for the period prior to the SSW event in January 2009 in the Northern Hemisphere. Thus, MV event includes such complicated nonlinear processes of troposphere-stratosphere dynamical coupling, which seems to be relatively difficult to predict. Hence, it is also considered that the development of error or the large spread area to the stratosphere in the unsuccessful experiments in Fig. 6-10 reflect failure of the reproduction of this coupling process. As a result, the predictability limits of the total ozone field based on PCC are longer than 10 days for ESV event, and about 6 days for MV event.

In MV event, we have also obtained the interesting result that the predictability limits are shorter for newer initial dates in Subsection 6.3. Such high initial-time sensitivity for the prediction seems to be related to the complicated dynamical coupling processes.

(a) ESV event

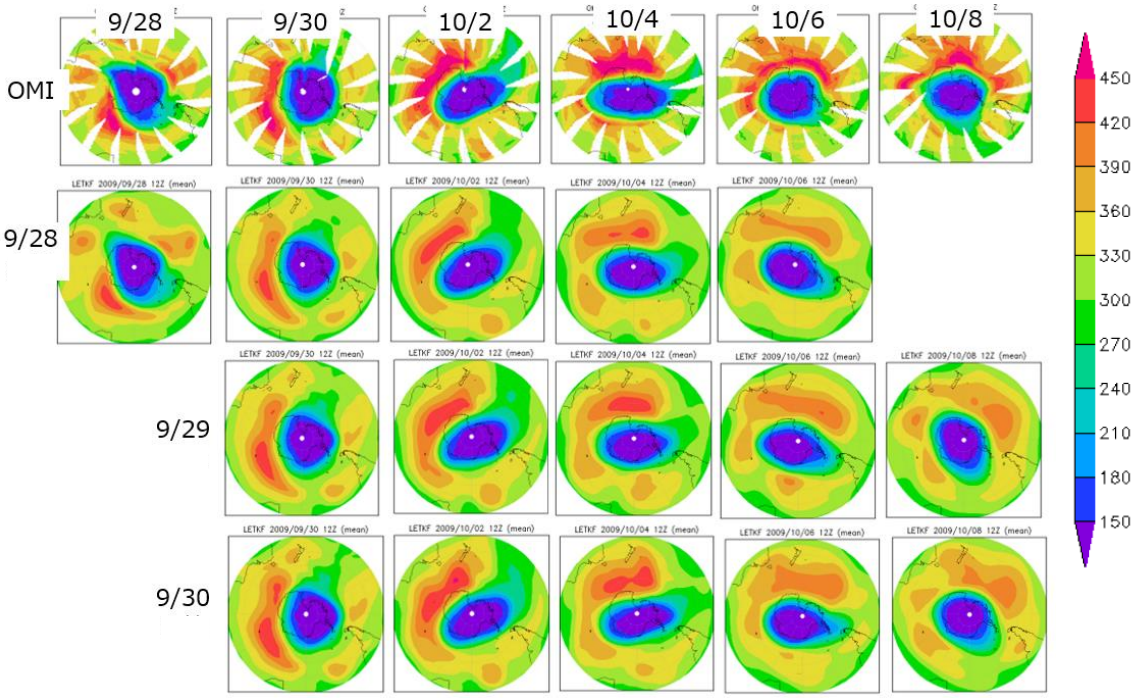

(b) MV event

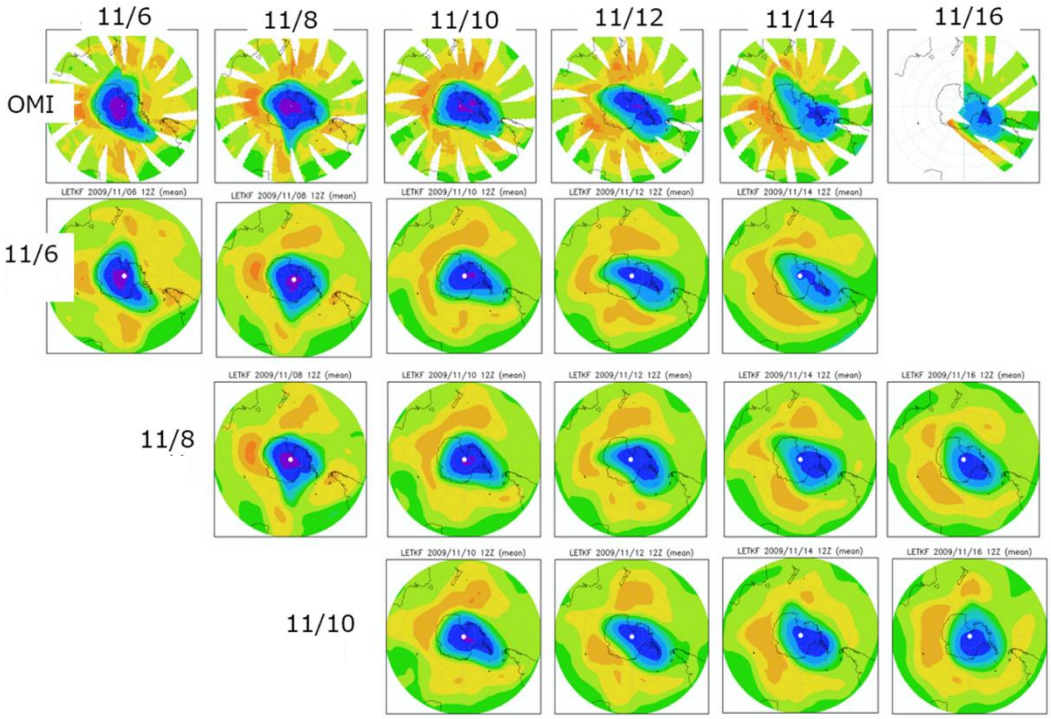

Figure 6-1: Total ozone maps in the Southern Hemisphere based on OMI observations (top panels) and ensemble mean of the forecast experiments for the periods of (a) 28 September - 8 October, 2009, (b) 6-16 November, 2009. Units are DU.

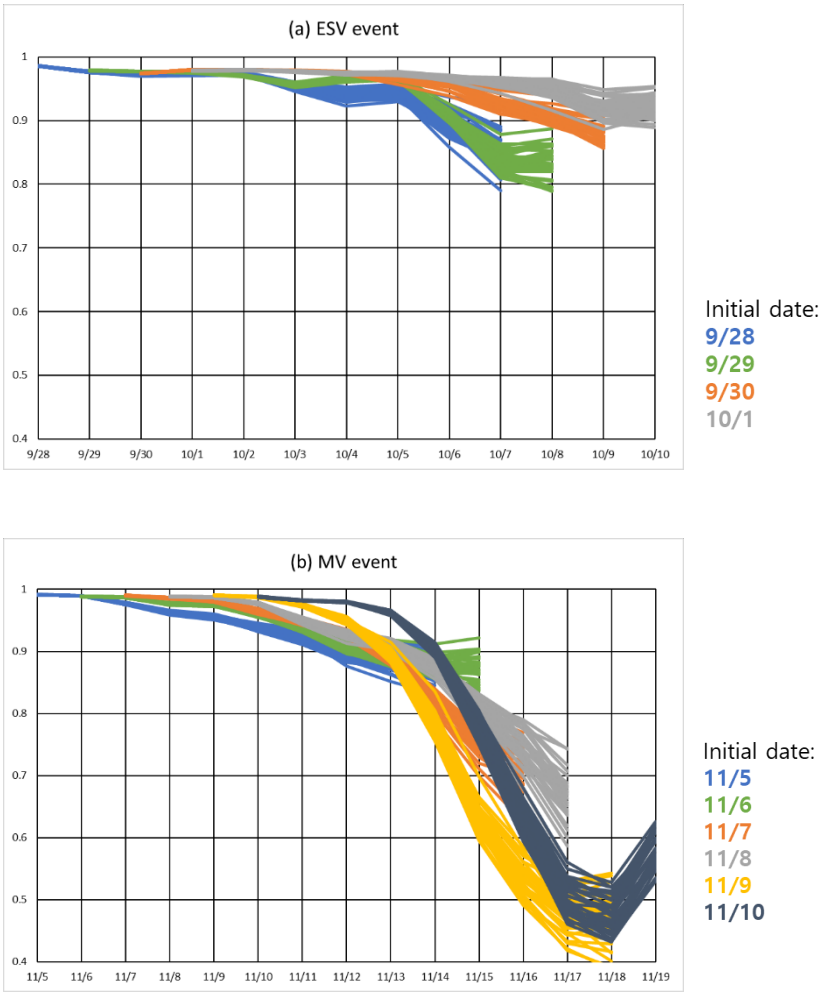

Figure 6-2: Time evolutions of total ozone PCC for 32 ensemble forecasts during the forecast period for (a) ESV event, (b) MV event.

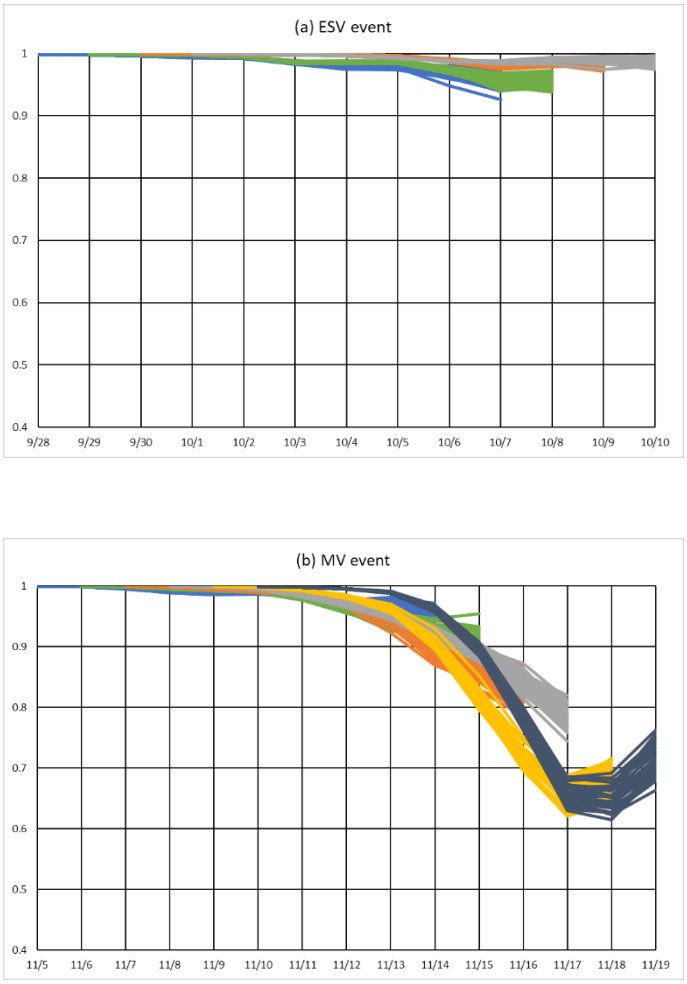

Figure 6-3: Same as Fig.6-2, but for 50 hPa geopotential height.

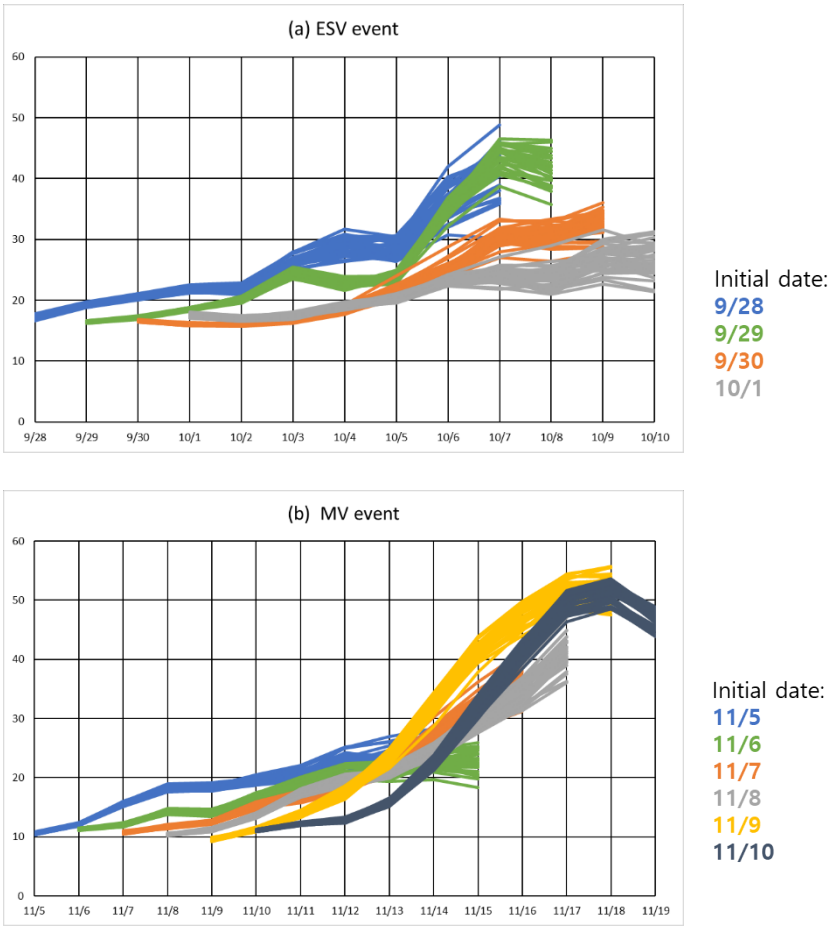

Figure 6-4: Time evolutions of the total ozone RMSE for the 32 ensemble forecasts during the forecast period for (a) ESV event, (b) MV event.

(a) wave number 1 (b) wave number 2

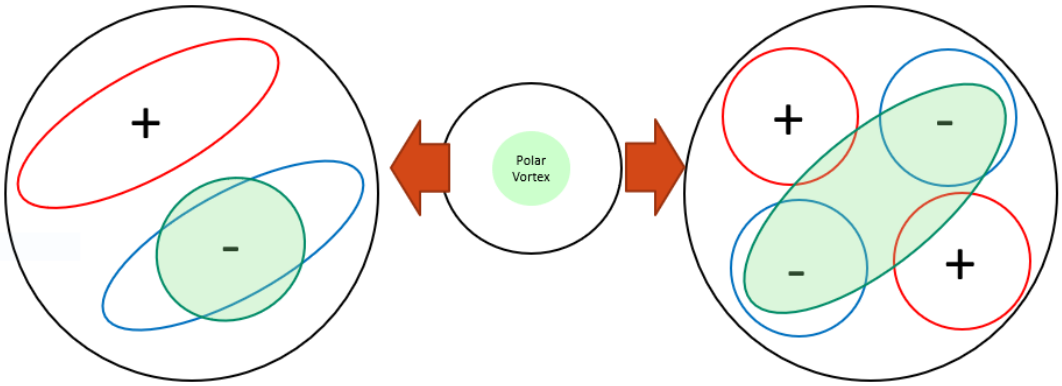

Figure 6-5: Schematic image of the responsibility between the polar vortex and planetary wave activity of (a) wave number 1 and (b) 2.

(a) Reanalysis (NIES CCM)

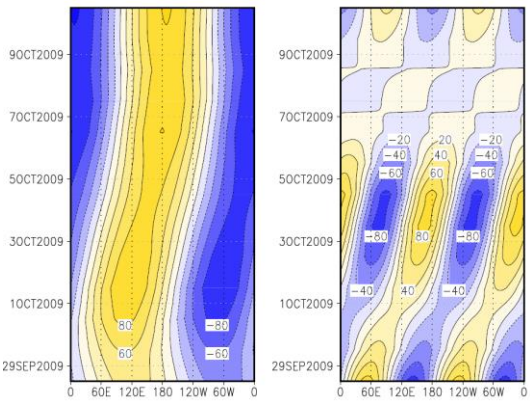

(b) Forecast (9/28-10/8)

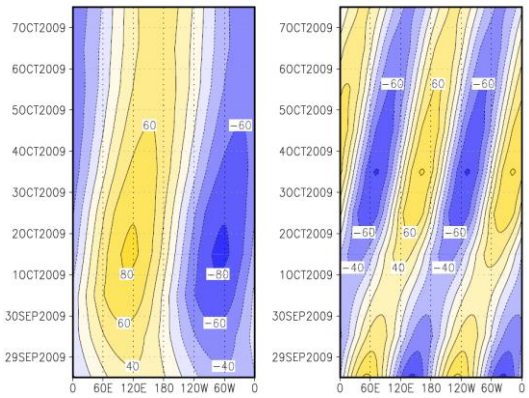

Figure 6-6: Hovmöller diagram of the wavenumber 1 (left panels) and 2 (right panels) components of total ozone at 60°S from 28 September to 10 October in 2009. (a) Reanalysis data calculated by NIES CCM and (b) Ensemble mean of the forecast experiments whose initial days are 28 September in 2009. Units are DU. The value of wave component is using yellow for positive values and blue for negative values.

(a) Reanalysis (NIES CCM)

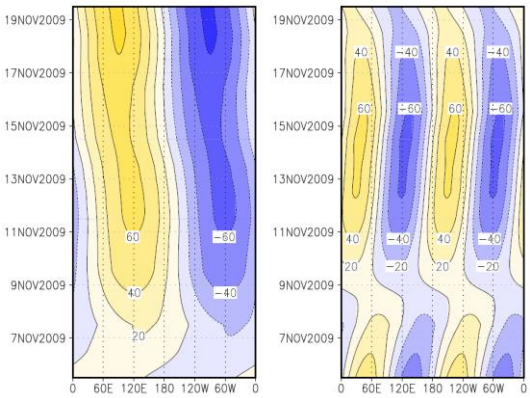

(b) Forecast (11/6-11/16)

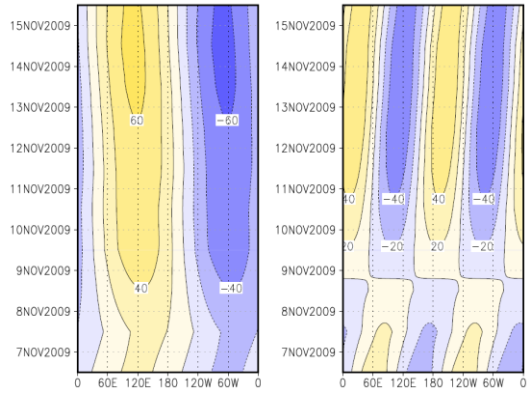

(c) Forecast (11/8-11/18)

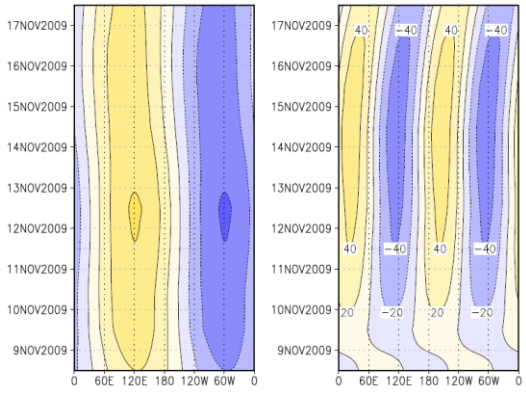

Figure 6-7: Same as Fig.6-6, but from 5 November to 20 November in 2009. (a) Reanalysis data calculated by NIES CCM and Ensemble mean of the forecast experiments whose initial days are (b) 6 November in 2009 and (c) 8 November in 2009.

(a) Reanalysis (NIES CCM)

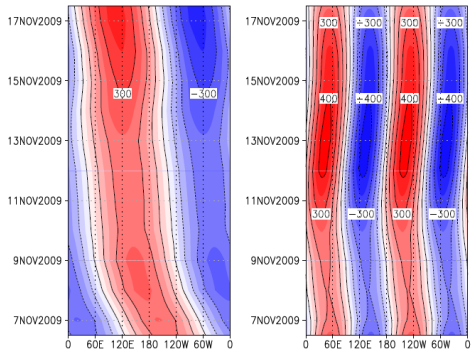

(b) Forecast (11/6-11/16)

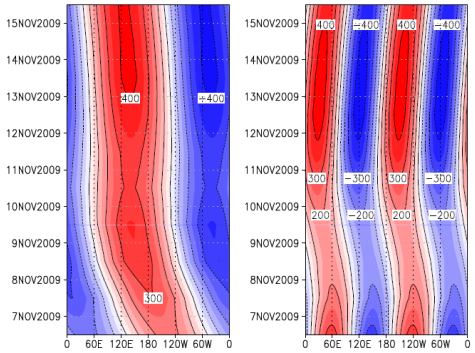

(c) Forecast (11/8-11/18)

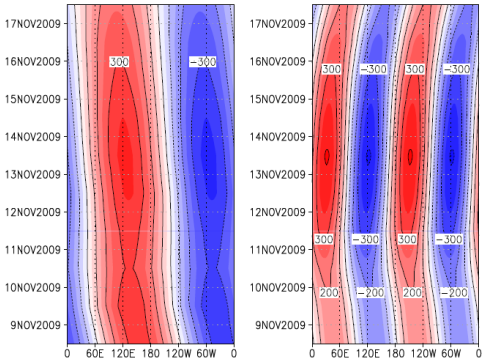

Figure 6-8: Same as Fig.6-7, but for the wavenumber 1 (left panels) and 2 (right panels) components of geopotential height at 60°S and 50 hPa. Units are m. The value of the wave component is indicated using red for positive values and blue for negative values.

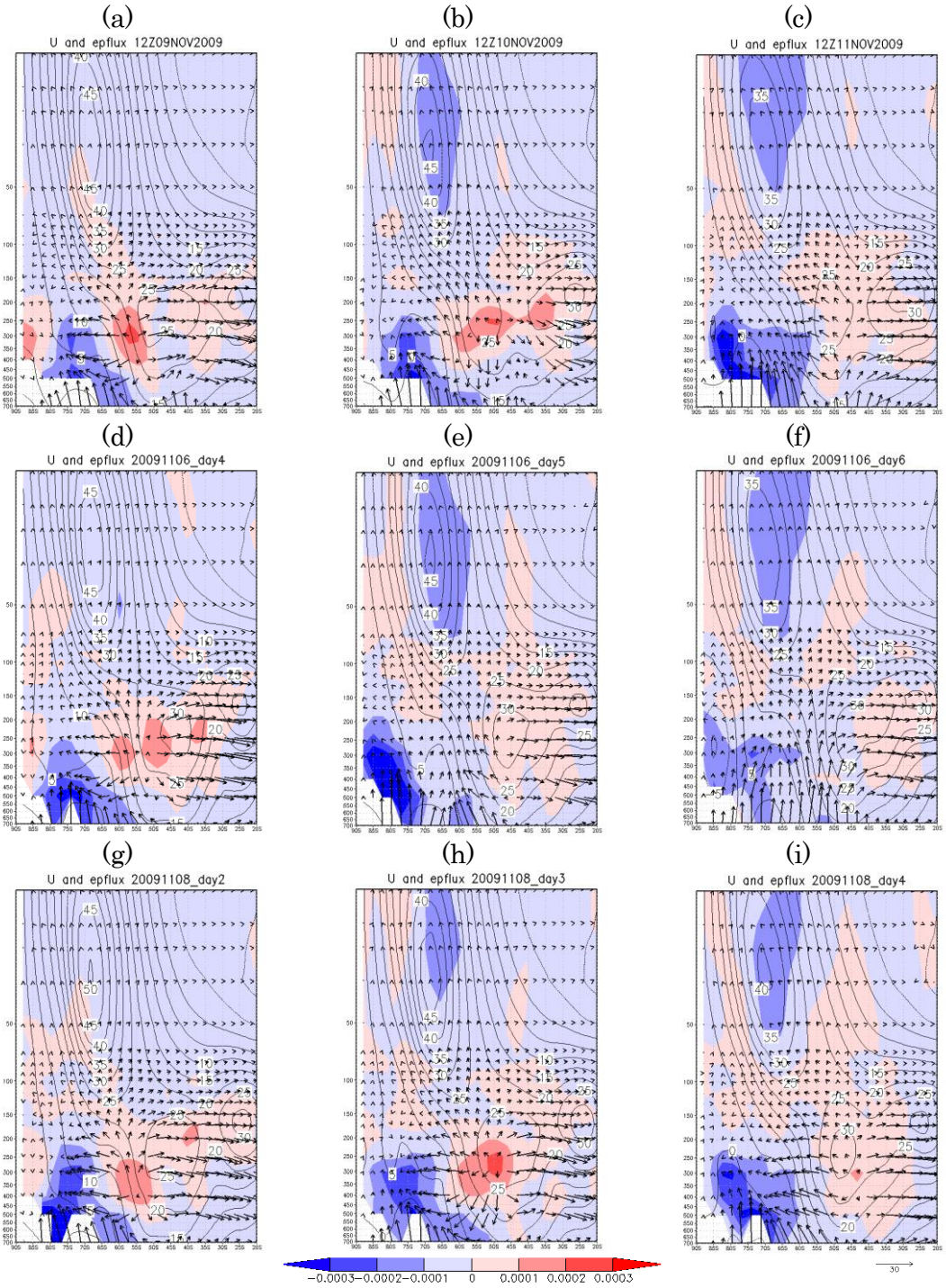

Figure 6-9: Latitude-height cross section of zonal mean zonal wind (contour), EP flux (vector), convergence of EP flux (ms^{-2}; color) for (a)-(c)analysis and forecast experiments whose initial dates are (d)-(f) 6 November in 2009 and (g)-(i) 8 November in 2009. (a)(d)(g) are on 9, (b)(e)(h) are on 10, (c)(f)(i) are on 11 November. The arrow at the bottom right denotes the scale of horizontal components of the EP flux vector ($kgm^{-1}s^{-2}$), and the vertical components are multiplied by 100.

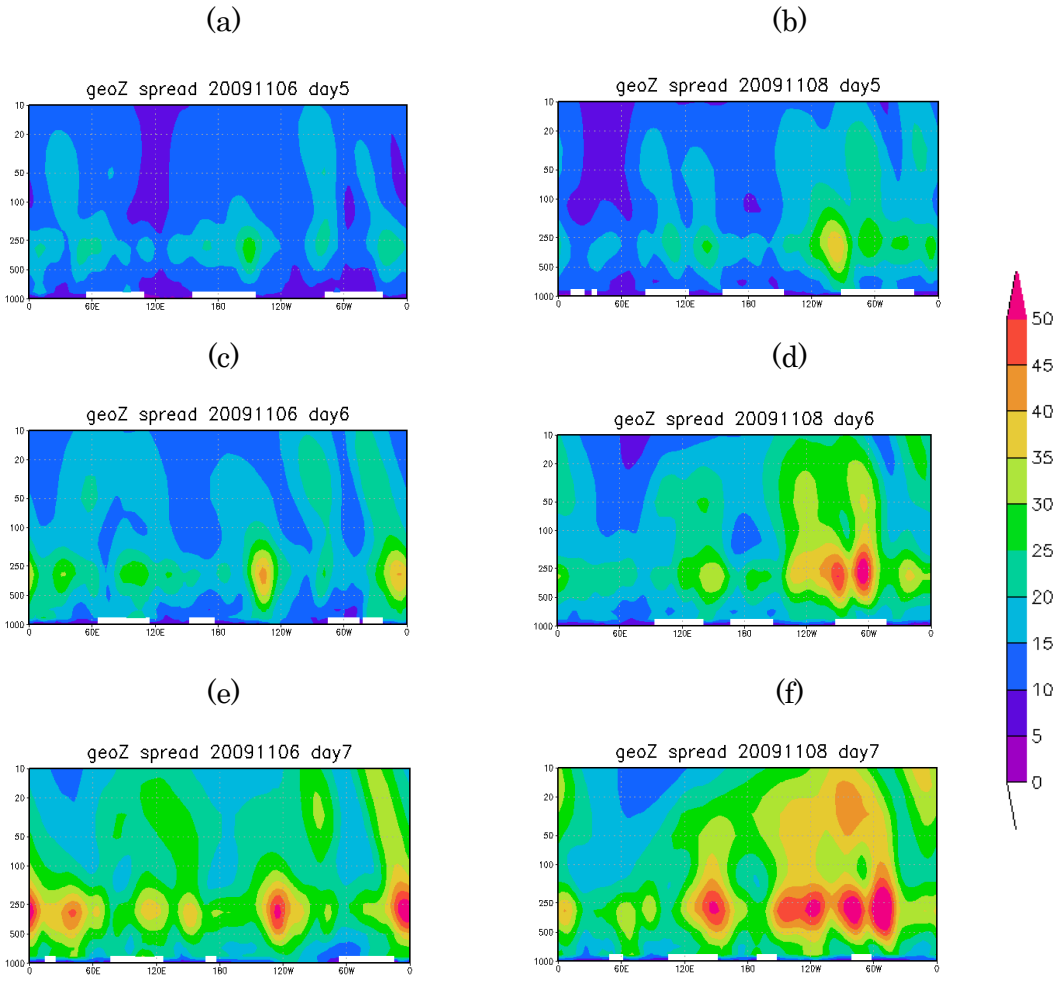

Figure 6-10: Longitude-height cross section of ensemble spreads of geopotential height averaged over 50°S to 70°S for the forecast experiments whose initial days are (a)(c)(e) 6 November in 2009 and (b)(d)(f) 8 November in 2009. Each panel indicates (a)(b) 5days, (c)(d) 6days and (e)(f) 7days after the initial days of forecast experiments. The values of spreads for geopotential height (m) are indicated by color.

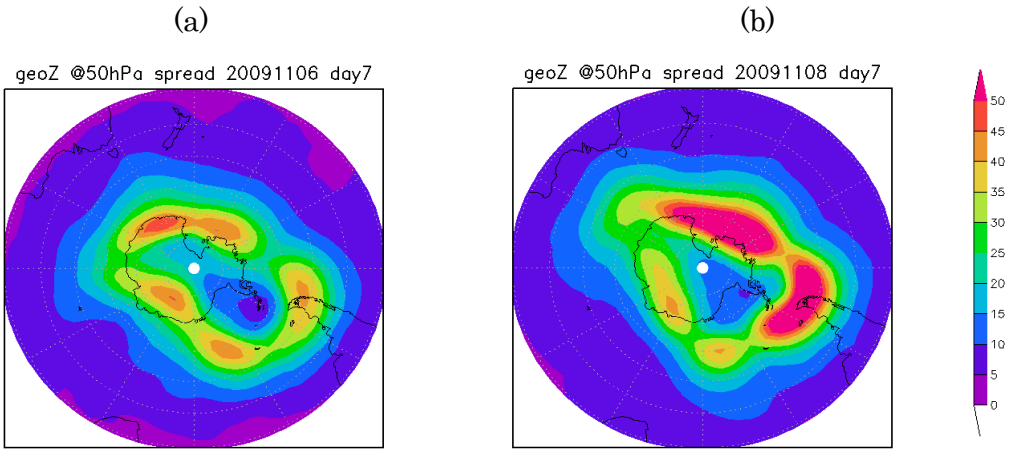

Figure 6-11: Polar map of ensemble spreads of geopotential height at 50 hPa for the forecast experiments whose initial days are (a) 6 November in 2009 and (b) 8 November in 2009. Each panel indicates 7days after the initial days of forecast experiments. The values of spreads for geopotential height (m) are indicated by color.

7. Concluding Remarks

In the present study, the stratospheric ozone predictability in the Southern Hemisphere spring has been examined using NIES CCM whose initial data has made by the ozone assimilated NIES CCM. It has been investigated on the basis of PCC and RMSE of the total ozone and the 50 hPa geopotential height for the two ozone reduction events in the Southern Hemisphere spring, 2009.

In the Southern Hemisphere spring, the polar vortex sometimes deformed elliptically by the wave activity and passed over southern tip of South America, then causes temporary total ozone reduction at the area. The predictability limit of total ozone field for such case is more than 10 days.

On the other hand, a reduction of the total ozone over the southern tip of South America lasting 3 weeks occurred in November 2009. The polar vortex distorted to an elliptic shape due to enhanced planetary wave activity, bringing to migration of the ozone depletion region associated with the Antarctic ozone hole towards the South American continent at the time of the vortex breakup. The predictability limit of the total ozone field for this event is about 6 days. The upward propagation of wave activity originating from the tropospheric blocking area raised error up to the stratosphere in the forecast experiments and this is considered to make difficult to

forecast this event.

Moreover, this study has also focused on the predictability for three types of assimilated data used by initial data. The forecast experiments with initial data to which dynamical fields are assimilated show higher total ozone than the observation. The experiments with initial data to which dynamical fields and ozone fields are assimilated show the ozone field close to the observation, although the difference of assimilated ozone data affect to the predictability limits. The predictability limit of the total ozone with initial data to which dynamical fields, total ozone fields and ozone profile are assimilated show the best predictability limit of about 12 days. On the other hand, the predictability limit for the total ozone with initial data to which dynamical fields and total ozone fields are assimilated is 9 days. This suggests importance of the accuracy of the ozone profile at the initial state.

Acknowledgements

I deeply appreciate to Prof. Toshihiko Hirooka at the Department of Earth Planetary Sciences at Kyushu University for his invaluable guidance and assistance. I express deep thanks to Dr. Hideharu Akiyoshi and Dr. Takafumi Sugita at National Institute for Environmental Studies and Prof. Akira Mizuno at Institute for Space-Earth Environment Research, Nagoya University, who gave me a chance to research the ozone reduction event through SATREPS project, for their kind advice and encouragement. I am grateful to Associate Prof. Yasunobu Miyoshi and Assosiate Prof. Takashi Mochizuki and Dr. Shunsuke Noguchi at the Department of Earth Planetary Sciences at Kyushu University for helpful discussions and valuable comments. I am grateful to Dr. Hisanori Itoh for his invaluable guidance and assistance during my master's course. My thanks are extended to Yuya Matsuyama and colleagues at Atmospheric and Geophysical Fluid Dynamics Laboratory during my doctor's course, and colleagues at Tropospheric Sciences Laboratory during my master's course for their supports and helpful discussions. I am grateful to Dr. Yosuke Yamashita at National Institute for Environmental Studies, Dr. Masanao Kadowaki at Japan Atomic Energy Agency for their supports and kind encouragement. I am grateful to Dr. Tetsu Nakamura at Japan Meteorological

Agency, who originally developed the Ozone Assimilated NIES CCM and advised me for extending the model. I appreciate to my colleagues in Fujitsu Japan Corporation for their encouragement. Finally, I express my deepest gratitude to my family for their support and encouragement.

The model calculations were performed by using the supercomputer system (NEC SX-ACE and NEC SX-Aurora TSUBASA) of the National Institute for Environmental Studies.

References

Andrews, D. G., J. R. Holton, and C. B. Leovy, 1987: *Middle Atmosphere Dynamics*, Academic, San Diego, Calif., 489 pp.

Andrews, D. G., and M. E. McIntyre, 1976: Planetary waves in horizontal and vertical shear: the generalized Eliassen-Palm relation and the mean zonal acceleration. *Journal of the Atmospheric Sciences,* **33**, 2031-2048.

Akiyoshi, H., L. B. Zhou, Y. Yamashita, K. Sakamoto, M. Yoshiki, T. Nagashima, M. Takahashi, J. Kurokawa,M. Takigawa, and T. Imamura, 2009: A CCM simulation of the breakup of the Antarctic polar vortex in the years 1980-2004 underthe CCMVal scenarios, *Journal of Geophysical Research*, **114**, D03103, doi:10.1029/2007JD009261

Akiyoshi, H., Kadowaki, M., Nakamura, H., Sugita, T., Hirooka, T., Harada, Y., and Mizuno, A. (2018). Analysis of the ozone reduction event over the southern tip of South America in November 2009. *Journal of Geophysical Research: Atmospheres,* **123**. doi:10.1029/2017JD028096.

Charney, J. G., and P. G. Drazin, 1961: Propagation of planetary-scale disturbances from the lower into the upper atmosphere. *Journal of Geophysical Research: Atmospheres*, **66**, 83-109.

de Laat, A. T. J., R. J. van der A, M. A. F. Allaart, M. van Weele, G. C. Benitez, C. Casiccia, N. M. Paes Leme, E. Quel, J. Salvador and E. Wolfram, 2010. Extreme sunbathing: Three weeks of small total O_3 columns and high UV radiation over the southern tip of South America during the 2009 Antarctic O_3 hole season. *Geophysical Research Letters*, **37**, L14805. doi: 10.1029/2010GL 043699.

Edmon Jr, H. J., B. J. Hoskins, M. E. McIntyre, 1980. Eliassen-Palm cross sections for the troposphere. *Journal of Atmospheric Sciences,* **37**(12), 2600-2616.

Eliassen, A., and E. Palm, 1961: On the transfer of energy in stationary mountain waves. *Geophysical Publications* **22**, 1-23.

Flemming, J., A. Inness, L. Jones, H. J. Eskes, V. Huijnen, M. G. Schultz, O. Stein, D. Cariolle, D. Kinnison, and G. Brasseur, 2011: Forecasts and assimilation experiments of the Antarctic ozone hole 2008. *Atmospheric Chemistry and Physics*, **11**, 1961–1977, doi:10.5194/acp-11-1961-2011.

Gelaro, R., W. McCarty, M. J. Suárez, R. Todling, A. Molod, L. Takacs, C. A. Randles, A. Darmenov, M. G. Bosilovich, R. Reichle, K. Wargan, L. Coy, R. Cullather, C. Draper, S. Akella, V. Buchard, A. Conaty, A. M. da Silva, W. Gu, G.-K. Kim, R. Koster, R. Lucchesi, D. Merkova, J. E. Nielsen, G. Partyka, S. Pawson, W. Putman, M. Rienecker, S. D. Schubert, M. Sienkiewicz, and B. Zhao, 2017: The

Modern-Era Retrospective Analysis for Research and Applications, Version 2 (MERRA-2), *J. Climate*, **30**, 5419–5454, https://doi.org/10.1175/JCLI-D-16-0758.1.

Harada, Y., A. Goto, H. Hasegawa, N. Fujikawa, H. Naoe, and T. Hirooka, 2010: A major stratospheric sudden warming event in January 2009. *Journal of the Atmospheric Sciences*, **67**, 2052–2069, doi:10.1175/2009JAS3320.1.

Hirooka, T., T. Ichimaru, and H. Mukougawa, 2007: Predictability of stratospheric sudden warmings as inferred from ensemble forecast data: Intercomparison of 2001/02 and 2003/04 winters. *Journal of Meteorological Society of Japan*, **85**, 919-925.

Hollingsworth, A., K. Arpe, M. Capaldo, H. Savijarvi, O. Akesson and J. A. Woods, 1978: Comparison of medium range forecasts made with two parameterization schemes. *ECMWF Tech, Rep.,* **13**, 214 pp.

Hunt, B. R., E. J. Kostelich, and I. Szunyogh 2007: Efficient data assimilation for spatiotemporal chaos: A local ensemble transform Kalman filter, *Physica D*, **230**, 112-126, doi:10.1016/j.physd.2006.11

Ichimaru, T., S. Noguchi, T. Hirooka, and H. Mukougawa, 2016: Predictability changes of stratospheric circulations in Northern Hemisphere winter. *Journal*

of Meteorological Society of Japan, **94**, 7-24, DOI:10.2151/jmsj.2016-001.

Kalnay, E., 2003: Atmospheric Modeling, Data Assimilation and Predictability. Cambridge University Press, 341 pp.

Kimoto, M., H. Mukougawa, and S. Yoden, 1992: Medium-range forecast skill variation and blocking transition: A case study. *Monthly Weather Review*, **120**, 1616-1627.

Kurokawa, J., H. Akiyoshi, T. Nagashima, H. Masunaga, T. Nagajima, M. Takahashi, and H. Nakane, 2005: Effects of atmospheric sphericity on stratospheric chemistry and dynamics over Antarctica, *Journal of Geophysical Research*, **110**, D21305, doi:10.1029/2005JD00

Kuroda, Y., 2008: Role of the stratosphere on the predictability of medium-range weather forecast: A case study of winter 2003-2004. *Geophysical Research Letters*, **35**, L19701, doi:10.1029/2008GL034902.

Kuroda, Y., 2010: High initial−time sensitivity of medium−range forecasting observed for a stratospheric sudden warming. *Geophysical Research Letters*, **37**, L16804, doi:10.1029/2010GL044119.

Livesey, N. J., W. G. Read, P. A. Wagner, L. Froidevaux, M. L. Santee, M. J. Schwartz, A. Lambert, L. F. Millán Valle, H. C. Pumphrey, G. L. Manney, R. A. Fuller, R. F.

Jarnot, B. W. Knosp, R. R. Lay, 2022: EOS MLS Version 5.0x Level 2 and 3 data quality and description document. Tech. Rep. JPL D-105336 Rev. B, Jet Propulsion Laboratory, Available from https://mls.jpl.nasa.gov/data/v5-0_data_quality_document.pdf.

McPeters, R., M. Kroon, G. Labow, E. Brinksma, D. Balis, I. Petropavlovskikh, J. P. Veefkind, P. K. Bhartia, and P. F. Levelt, 2008: Validation of the Aura Ozone Monitoring Instrument total column ozone product. J. Geophys. Res., **113**, D15S14, doi:10.1029/2007JD008802.

Miyoshi, T., and S. Yamane, 2007: Local ensemble transform Kalman filtering with an AGCM at a T159/L48 resolution, *Monthly Weather Review*, **135**, 3841-3861, doi:10.1175/2007MWR18

Mukougawa, H., and T. Hirooka, 2004: Predictability of stratospheric sudden warming: A case study for 1998/99 winter. *Monthly Weather Review*, **132**, 1764-1776.

Mukougawa, H., H. Sakai, T. Hirooka, 2005: High sensitivity to the initial condition for the prediction of stratospheric sudden warming. *Geophysical Research Letters*, **32**, L17806, doi:10.1029/2005GL022909.

Nakamura, T., H. Akiyoshi, M. Deushi, K. Miyazaki, C. Kobayashi, K. Shibata, and

T. Iwasaki, 2013, A multimodel comparison of stratospheric ozone data assimilation based on an ensemble Kalman filter approach, *Journal of Geophysical Research: Atmospheres*,**118**, 3848-3868, doi:10.1002/jgrd.50338

Noguchi, S., H. Mukougawa, T. Hirooka, M. Taguchi, and S. Yoden, 2014: Month-to-month predictability variations of the winter-time stratospheric polar vortex in an operational one-month ensemble prediction system. *Journal of Meteorological Society of Japan*, **92**, 543-558.

Noguchi, S., H. Mukougawa, Y. Kuroda, R. Mizuta, S. Yabu, and H. Yoshimura 2016: Predictability of the strato-spheric polar vortex breakdown: An ensemble reforecast experiment for thesplitting event in January 2009, *Journal of Geophysical Research: Atmospheres*, **121**, 3388-3404, doi:10.1002/2015JD024

Nishii, K., H. Nakamura, and Y. J. Orsolini, 2011: Geographical dependence observed in blocking high influence on the stratospheric variability through enhancement and suppression of upward planetary-wave propagation. *Journal of Climate*, **24**(24), 6408–6423. doi:10.1175/JCLI-D-10-05021.

Rao, J., Garfinkel, C. I., Chen, H., and White, I. P., 2019: The 2019 New Year stratospheric sudden warming and its real–time predictions in multiple S2Smodels. *Journal of Geophysical Research: Atmospheres*, **124**, doi:

10.1029/2019JD030826

Sekiyama, T. T., and K. Shibata, 2005: Predictability of total ozone using a global three-dimensional chemical transport model coupled with the MRI/JMA98 GCM. *Monthly Weather Review*, **133**, 2262–2274, doi:10.1175/MWR2976.1.

Stan, C., and M. Straus, 2009: Stratospheric predictability and sudden stratospheric warming events. *Journal of Geophysical Research*, **114**, L12103, doi:10.1029/2008JD011277.

WMO (World Meteorological Organization), 2018: Scientific Assessment of Ozone Depletion: 2018. Global Ozone Research and Monitoring Project – Report No. 58, 588 pp., Geneva, Switzerland.

Wolfram, E. A., Salvador, J., Orte, F., D'Elia, R., Godin-Beekmann, S., Kuttippurath, J., Pazmino, A., Goutail, F., Casiccia, C., Zamorano, F., Paes Leme, N., and Quel, E. J. 2012: The unusual persistence of an ozone hole over a southern mid-latitude station during the Antarctic spring 2009: A multi-instrument study. *Annales Geophysicae,* **30** (10), 1435-1449. doi:10.5194/angeo-30-1435-2012.